



Two-scale Analysis of Solar Magnetic Helicity

Axel Brandenburg^{1,2,3,4}, Gordon J. D. Petrie⁵, and Nishant K. Singh³

¹Laboratory for Atmospheric and Space Physics, University of Colorado, Boulder, CO 80303, USA; brandenb@nordita.org

²JILA and Department of Astrophysical and Planetary Sciences, University of Colorado, Boulder, CO 80303, USA

³Nordita, KTH Royal Institute of Technology and Stockholm University, Roslagstullsbacken 23, SE-10691 Stockholm, Sweden

⁴Department of Astronomy, AlbaNova University Center, Stockholm University, SE-10691 Stockholm, Sweden

⁵National Solar Observatory, 3665 Discovery Drive, Boulder, CO 80303, USA

Received 2016 October 17; revised 2016 December 26; accepted 2016 December 31; published 2017 February 6

Abstract

We develop a two-scale formalism to determine global magnetic helicity spectra in systems where the local magnetic helicity has opposite signs on both sides of the equator, giving rise to cancellation with conventional methods. We verify this approach using first a synthetic one-dimensional magnetic field and then two-dimensional slices from a three-dimensional α effect-type dynamo-generated magnetic field, with forced turbulence of opposite helicity above and below the midplane of the domain. We then apply this formalism to global solar synoptic vector magnetograms. To improve the statistics, data from three consecutive Carrington rotations (2161–2163) are combined into a single map. We find that the spectral magnetic helicity representative of the northern hemisphere is negative at all wavenumbers and peaks at $\approx 0.06 \text{ Mm}^{-1}$ (scales around 100 Mm). There is no evidence of bihelical magnetic fields that are found in three-dimensional turbulence simulations of helicity-driven α effect-type dynamos.

Key words: dynamo – magnetohydrodynamics (MHD) – Sun: magnetic fields – turbulence

1. Introduction

Magnetic helicity is a conserved quantity not only in ideal magnetohydrodynamics (MHD), but also in nonideal MHD in the limit of large magnetic Reynolds numbers. It plays a crucial role in the theory of astrophysical large-scale dynamos, given that in many cosmic bodies, the magnetic Reynolds numbers are very large indeed. Dynamo theory is relevant to explaining the global cyclic magnetic field of the Sun (Kleeorin & Ruzmaikin 1982; Gruzinov & Diamond 1996; Brandenburg 2001; Field & Blackman 2002). Magnetic helicity is also a topological invariant characterizing the linkage of magnetic field lines and thus its complexity. Large values of magnetic helicity appear to be connected with the launching of coronal mass ejections (Low 1994; Nindos et al. 2003; Amari et al. 2014), which in turn are relevant to understanding space weather. This led to the quantitative evaluation of magnetic helicity in volumes above the solar surface around active regions (ARs); see Pariat et al. (2015) for recent work.

To make contact with possible mechanisms that generate helical magnetic fields, it is necessary to decompose magnetic helicity into contributions from different length scales. It has been known for some time that the α effect produces a so-called bihelical magnetic field, with opposite signs at small and large wavenumbers (Seehafer 1996; Ji 1999; Blackman & Brandenburg 2003). At each position, the net helicity integrated over contributions from all scales is then actually zero. Thus, to make meaningful quantitative statements, one needs to compute magnetic helicity *spectra*; see Yousef and Brandenburg (2003) for examples of such fields produced by the α effect.

As a preliminary means of obtaining information about the magnetic helicity of the large-scale field, one can use the azimuthally averaged magnetic field to compute $2\bar{A}_\phi\bar{B}_\phi$, where \bar{A}_ϕ is the mean toroidal vector potential and \bar{B}_ϕ is the mean toroidal magnetic field. By taking the sign of \bar{B}_ϕ using Hale's polarity law and computing \bar{A}_ϕ from the spherical harmonics

decomposition of the mean radial magnetic field, Brandenburg et al. (2003) concluded that, in the northern hemisphere, $\bar{A}_\phi\bar{B}_\phi$ was negative (positive) before (after) solar maximum. A similar dependence was also obtained by Zhang et al. (2010) by measuring the current helicity. Using synoptic vector magnetograms, Pipin and Pevtsov (2014) computed \bar{A}_ϕ and \bar{B}_ϕ to obtain the global magnetic helicity of the large-scale field of the Sun. They found positive magnetic helicity in the north and negative in the south, as expected from dynamo theory.

Magnetic helicity spectra are similar to magnetic energy spectra, which have been computed for the Sun for some time (Nakagawa & Priest 1973; Abramenko 2005; Stenflo 2012). Magnetic helicity spectra can be computed analogously, but this has only recently been attempted (Zhang et al. 2014, 2016). Those spectra can be of different signs in different wavenumber ranges and at different positions on the solar surface. Particularly important for the solar dynamo is the possibility of a systematic dependence on solar latitude. The question therefore arises as to how to analyze and present such complex dependencies on position and scale in an efficient way.

A simple approach would be to determine spectra in different local patches, but this can only be meaningful if the patches are not too large. This is indeed what has been done in the work of Zhang et al. (2014, 2016), who used patches of $(186 \text{ Mm})^2$. However, a more elaborate technique has been developed in mean-field dynamo theory by Roberts and Soward (1975) to separate large and small scales. This is generally referred to as *two-scale analysis*. It involves a so-called double Fourier transform, and allows one to compute quadratic small-scale correlations such as the mean electromotive force at large scales as a function of position based on Fourier transforms of the constituent fields. This is particularly important if the large length scales of interest are not just the full spatial extent (corresponding to zero wavenumber), but a somewhat smaller scale (finite wavenumber) on which physical properties of the system vary slowly. This is relevant to the Sun, where one can

expect statistically similar conditions at all longitudes, but only within broad bands in latitude. Regarding the helicity of the magnetic field, for example, one expects opposite signs in the northern and southern hemispheres (e.g., Pevtsov et al. 2008, 2014), so one would obtain zero when averaging over north and south.

In this paper we begin by demonstrating the properties of the double Fourier transform. We consider first simple one-dimensional (1D) helical and bihelical magnetic fields in the presence of an equator, where the helicity changes sign. Next, we apply the two-scale analysis to a three-dimensional (3D) turbulent dynamo with periodic boundary conditions and an equator in the middle that cuts the domain into two halves, with opposite helicity of the forcing function. Finally, we employ full-disk vector magnetograms from the Helioseismic and Magnetic Imager (HMI) on board the *Solar Dynamics Observatory (SDO)* to obtain all three magnetic field components at the two-dimensional (2D) surface of the Sun, to compute magnetic helicity spectra from a sequence of synoptic maps.

2. Formalism

2.1. The Usual Magnetic Energy and Helicity Spectra

In a periodic Cartesian domain, the usual magnetic energy spectrum is given by the integral over shells in wavenumber space of the Fourier-transformed magnetic energy density,

$$E_M(k) = \int_{\Omega_D} \frac{1}{2} \hat{\mathbf{B}}(\mathbf{k}) \cdot \hat{\mathbf{B}}^*(\mathbf{k}) k^{D-1} d\Omega, \quad (1)$$

where $d\Omega$ is the surface differential in Fourier space in D dimensions. In $D = 3$ dimensions, the surface of a D -dimensional unit sphere is $\Omega_3 = 4\pi$. In $D = 2$ dimensions, $\Omega_2 = 2\pi$ is the circumference of a unit circle, while in $D = 1$ dimensions, $\Omega_1 = 2$ corresponds to the two end points of a line. Here and in the following discussion, we measure the magnetic energy density in G^2 rather than $J m^{-3}$, so the vacuum permeability factor is dropped. Furthermore, $k = |\mathbf{k}|$ is the radius of a sphere in Fourier space, and hats denote the Fourier transform of the magnetic field, that is,

$$\hat{\mathbf{B}}(\mathbf{k}) = \int \mathbf{B}(\mathbf{x}) e^{-i\mathbf{k}\cdot\mathbf{x}} d^Dx / (2\pi)^D. \quad (2)$$

The magnetic helicity spectrum is defined analogously to $E_M(k)$ as

$$H_M(k) = \int_{\Omega_D} \frac{1}{2} [\hat{\mathbf{A}} \cdot \hat{\mathbf{B}}^* + \hat{\mathbf{A}}^* \cdot \hat{\mathbf{B}}] k^{D-1} d\Omega, \quad (3)$$

where $\hat{\mathbf{A}}(\mathbf{k})$ is the Fourier transform of the vector potential $\mathbf{A}(\mathbf{x})$, with $\nabla \times \mathbf{A} = \mathbf{B}$ and $\hat{\mathbf{B}} = i\mathbf{k} \times \hat{\mathbf{A}}$. These spectra are normalized such that

$$\int_0^\infty E_M(k) dk = \frac{1}{2} \langle \mathbf{B}^2 \rangle_V \equiv \mathcal{E}_M, \quad (4)$$

$$\int_0^\infty H_M(k) dk = \langle \mathbf{A} \cdot \mathbf{B} \rangle_V \equiv \mathcal{H}_M, \quad (5)$$

where angle brackets with subscript V denote volume averages. Analogously, one can define the current helicity spectrum $H_C(k)$ such that $\int H_C(k) dk = \langle \mathbf{J} \cdot \mathbf{B} \rangle_V$, where $\mathbf{J} = \nabla \times \mathbf{B}$ is proportional to the current density.

For the following, it is useful to remember that the magnetic energy spectrum is the Fourier transform of the trace of the two-point correlation tensor

$$M_{ij}(\mathbf{x}) = \int \langle B_i(\mathbf{X}) B_j(\mathbf{X} + \mathbf{x}) \rangle d^D\mathbf{X}, \quad (6)$$

where angle brackets denote ensemble averaging, which could be approximated by averaging over time, and $M_{ij}(\mathbf{x})$ is assumed to be statistically independent of \mathbf{X} , owing to the assumption of homogeneity. Thus, following standard relationships (e.g., Matthaeus et al. 1982; Brandenburg et al. 2011), the energy spectrum is then given by $2E_M(k) = \int \delta_{ij} \hat{M}_{ij}(\mathbf{k}) k^{D-1} d\Omega$, where $\hat{M}_{ij}(\mathbf{k}) = \int M_{ij}(\mathbf{x}) e^{-i\mathbf{k}\cdot\mathbf{x}} d^Dx / (2\pi)^D$ is the Fourier transform of M_{ij} . Likewise, the scaled magnetic helicity spectrum is given by $kH_M(k) = \int i\hat{k}_i \epsilon_{ijk} \hat{M}_{jk}(\mathbf{k}) k^{D-1} d\Omega$, where $\hat{k}_i = k_i / |\mathbf{k}|$ is the unit vector of \mathbf{k} . (The hat on \mathbf{k} is not to be confused with the hats on \mathbf{B} or M_{ij} , where they denote Fourier transforms over \mathbf{k} .) (Including here the factors 2 and k on the left sides of the two equations has the advantage that $2E_M(k)$ and $kH_M(k)$ thus have the same prefactors.) Note that under isotropic conditions, $k^2 H_M(k) = H_C(k)$. Such spectra show the high-wavenumber range better than just $H_M(k)$ or $kH_M(k)$, and are therefore also considered in some of the following cases.

The magnetic helicity spectrum can be defined analogously from a tensorial generalization of the magnetic two-point correlation tensor. This will be done in the following section, where we will also relax the assumption of homogeneity and allow the spectra to be slowly varying functions of \mathbf{X} .

2.2. Double Fourier Transform

To obtain magnetic energy and helicity spectra that vary slowly in space, we consider the two-point correlation tensor at position \mathbf{X} (Roberts & Soward 1975),

$$M_{ij}(\mathbf{X}, \mathbf{x}) = \left\langle B_i\left(\mathbf{X} + \frac{1}{2}\mathbf{x}\right) B_j\left(\mathbf{X} - \frac{1}{2}\mathbf{x}\right) \right\rangle, \quad (7)$$

where \mathbf{x} is the distance between two points around \mathbf{X} . This expression is similar to Equation (6), except that the dependence on the slowly varying coordinate \mathbf{X} has been retained and the two points of the two-point correlation function are now symmetric about \mathbf{X} . In the following, we refer to such an analysis involving dependencies on both \mathbf{x} and \mathbf{X} as a two-scale approach. Sometimes we refer to this also as a global approach, as opposed to the local approach involving smaller patches within just one hemisphere, as done in Zhang et al. (2014, 2016).

By performing a Fourier transformation over \mathbf{x} , we obtain

$$\hat{M}_{ij}(\mathbf{X}, \mathbf{k}) = \int M_{ij}(\mathbf{X}, \mathbf{x}) e^{-i\mathbf{k}\cdot\mathbf{x}} d^Dx / (2\pi)^D \quad (8)$$

for the spectral correlation tensor. The symmetric part of this tensor contains information about the energy spectrum, and the anti-symmetric components contain information about the magnetic helicity spectrum. Under isotropic conditions, $\hat{M}_{ij}(\mathbf{X}, \mathbf{k})$ can be represented as

$$\hat{M}_{ij} = [(\delta_{ij} - \hat{k}_i \hat{k}_j) 2E_M - i\hat{k}_k \epsilon_{ijk} kH_M] / 2k^{D-1} \Omega_D, \quad (9)$$

and the magnetic energy spectrum is given by

$$2E_M(\mathbf{X}, k) = \int_{\Omega_D} \delta_{ij} \hat{M}_{ij}(\mathbf{X}, \mathbf{k}) k^{D-1} d\Omega, \quad (10)$$

while the magnetic helicity spectrum (scaled with k) is given by (Roberts & Soward 1975)

$$kH_M(\mathbf{X}, k) = \int_{\Omega_D} i\hat{k}_i \epsilon_{ijk} \hat{M}_{jk}(\mathbf{X}, \mathbf{k}) k^{D-1} d\Omega. \quad (11)$$

Except for the \mathbf{X} dependence, this formula is equivalent to that used to estimate magnetic helicity in the solar wind (Matthaeus et al. 1982; Brandenburg et al. 2011) and at the solar surface (Zhang et al. 2014, 2016); see also the end of Section 2.1.

In practice, we are interested in the case where the helicity varies in latitude and changes sign at the equator. Before discussing the magnetic field at the surface of the Sun, where the field is given in spherical coordinates, we consider examples in Cartesian coordinates. This is technically and conceptionally easier. We consider a cubic domain of size L^3 , which is homogeneous in the x and y directions, but inhomogeneous in the z direction, such that $0 \leq z \leq \pi$ corresponds to the northern hemisphere and $-\pi \leq z \leq 0$ to the southern. We are interested in slow changes of the magnetic energy and helicity spectra as a function of $\mathbf{X} = (X, Y, Z)$, where we shall be specifically interested in the dependence on Z , which corresponds to latitude or distance from the equator or the midplane. This can easily be done by performing an additional Fourier transform over \mathbf{X} :

$$\tilde{M}_{ij}(\mathbf{K}, \mathbf{k}) = \int \hat{M}_{ij}(\mathbf{X}, \mathbf{k}) e^{-i\mathbf{K}\cdot\mathbf{X}} d^D\mathbf{X} / (2\pi)^D. \quad (12)$$

It can then be shown that (Roberts & Soward 1975)

$$\tilde{M}_{ij}(\mathbf{K}, \mathbf{k}) = \left\langle \hat{B}_i \left(\mathbf{k} + \frac{1}{2}\mathbf{K} \right) \hat{B}_j^* \left(\mathbf{k} - \frac{1}{2}\mathbf{K} \right) \right\rangle. \quad (13)$$

Thus slow variations of the spectrum correspond to a shift between two points in wavenumber space. By integrating again over ‘‘shells’’ in \mathbf{k} space, we obtain \mathbf{K} -dependent magnetic energy and helicity spectra analogously to Equations (10) and (11) as

$$2\tilde{E}_M(\mathbf{K}, k) = \int_{\Omega_D} \delta_{ij} \tilde{M}_{ij}(\mathbf{K}, \mathbf{k}) k^{D-1} d\Omega, \quad (14)$$

$$k\tilde{H}_M(\mathbf{K}, k) = \int_{\Omega_D} i\hat{k}_i \epsilon_{ijk} \tilde{M}_{jk}(\mathbf{K}, \mathbf{k}) k^{D-1} d\Omega. \quad (15)$$

Thus the spectrum of magnetic helicity with a slow variation in the z direction is proportional to $\sin K_Z Z$ and is given by $\mathbf{K} = (0, 0, K_Z)$, where $K_Z = 2\pi/L$ and $z = Z$ are used interchangeably.

Unlike $H_M(\mathbf{X}, k)$, which is real, $\tilde{H}_M(\mathbf{K}, k)$ is complex. The quantity of interest depends on the spatial profile of the background helicity. For the rest of this paper, we are concerned with helicity profiles proportional $\sin K_0 Z$ with an equator at $Z = 0$. Its Fourier transform is $-\frac{1}{2}i\delta(K_Z - K_0)$. We will therefore plot the *negative imaginary part* of $\tilde{H}_M(\mathbf{K}, k)$, which reflects the sign of magnetic helicity in the northern hemisphere.

3. Testing the Formalism

To verify that the two-scale formalism allows us to disentangle the proper magnetic helicity from measurements

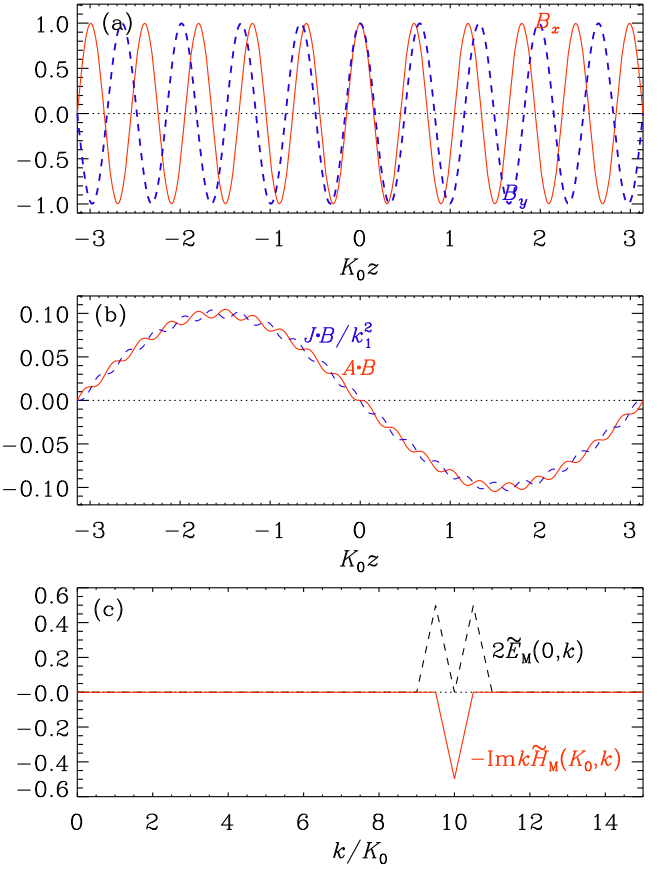


Figure 1. (a) $B_x(z)$ and $B_y(z)$ from Equation (16) with $k_1/K_0 = -10$, (b) $\mathbf{A} \cdot \mathbf{B}$ and $\mathbf{J} \cdot \mathbf{B}/k_1^2$, as well as (c) $2\tilde{E}_M(0, k)$ and $k\tilde{H}_M(K_0, k)$.

over the full domain, and thus both hemispheres, we apply it first to data where we know the result: (i) a synthetically constructed 1D helical Beltrami-like magnetic field and (ii) a 3D field from a turbulent dynamo with a hemispheric modulation of the helicity of the forcing function.

3.1. A 1D Example

A simple static 1D helical magnetic field is a Beltrami field of the form $\mathbf{B} = (\sin k_1 z, \cos k_1 z, 0)$, but its magnetic helicity density is uniform, because in this example, the vector potential is parallel to \mathbf{B} with $\mathbf{A} = \mathbf{B}/k_1$. Here k_1 is the wavenumber of the magnetic field, and the helicity is positive for $k_1 > 0$ and is associated with a $\pi/2$ phase shift where B_y precedes B_x as a function of z by a phase shift of $\pi/2$.

To make the helicity density a slowly varying function of z , the phase shift between B_x and B_y must also slowly change. This is accomplished by having slightly different wavenumbers for B_x and B_y . Equation (13) suggests the following form

$$\mathbf{B} = (\cos k_1^- z, \cos k_1^+ z, 0), \quad (16)$$

where $k_1^\pm = k_1 \pm \frac{1}{2}K_0$ and K_0 is the wavenumber of the slowly varying magnetic helicity density; see Figure 1(a). The corresponding vector potential is $\mathbf{A} = ((k_1^+)^{-1} \sin k_1^+ z, -(k_1^-)^{-1} \sin k_1^- z, 0)$, so the magnetic helicity density is then obtained as

$$\mathbf{A} \cdot \mathbf{B} = \left(k_1 \sin K_0 z - \frac{1}{2} K_0 \sin 2k_1 z \right) / \left(k_1^2 - \frac{1}{4} K_0^2 \right). \quad (17)$$

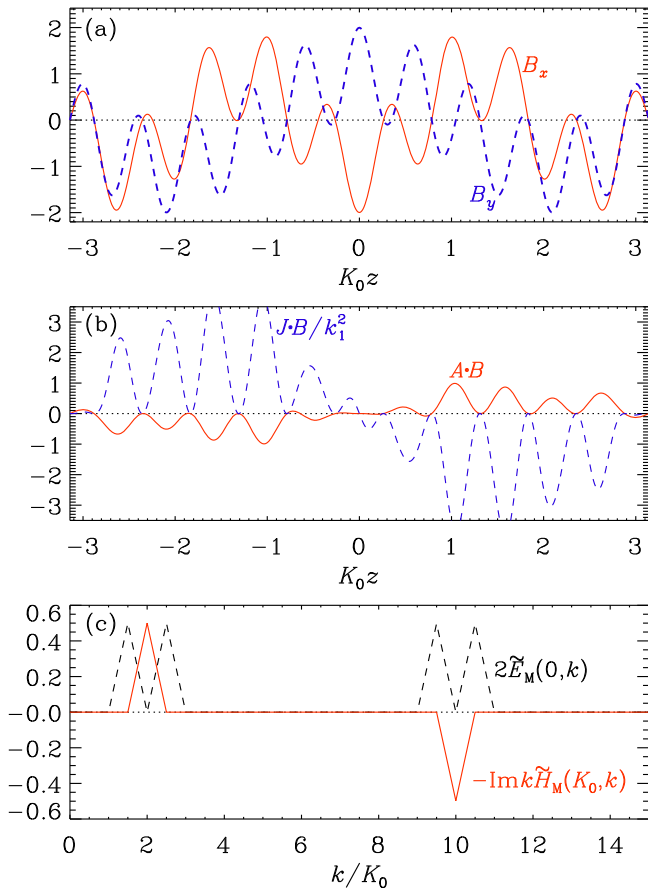


Figure 2. Similar to Figure 1, but for a bihelical field with $k_1/K_0 = 2$ and $k_2/K_0 = -10$.

For $k_1 \gg K_0$, we have $\mathbf{A} \cdot \mathbf{B} \approx k_1^{-1} \sin K_0 z$; see also Figure 1(b). As shown in detail in Appendix, the magnetic energy spectrum at $K = 0$ is

$$2\tilde{E}_M(0, k) = \frac{1}{2}(\delta_k k_1^+ + \delta_k k_1^-) \quad (18)$$

and the magnetic helicity spectrum at $K = K_0$ is

$$-\text{Im}k\tilde{H}_M(K_0, k) = \frac{1}{2} \text{sgn } k_1 \delta_k k_1 \quad (19)$$

(see Figure 1(c)). Thus the presence of small-scale helicity with a $K = K_0$ modulation is perfectly captured by the two-scale analysis. In particular, the sign of $-\text{Im}k\tilde{H}_M(K_0, k)$ is equal to the sign of the magnetic helicity in the northern hemisphere, and thus equal to the sign of k_1 .

Next we demonstrate in Figure 2 that even a bihelical magnetic field consisting of a superposition of two helical magnetic fields with different wavenumbers and opposite signs can still easily be disentangled, even though the helicities of both components are already modulated and change sign proportional to $\sin K_0 z$. In this case, the spatial profiles of $\mathbf{A} \cdot \mathbf{B}$ and $\mathbf{J} \cdot \mathbf{B}$ are no longer related to each other in a simple way and tend to have opposite signs (see Figure 2(b)).

3.2. 3D Turbulence

We now consider the results for helically forced 3D hydromagnetic turbulence in triply periodic domains. The forcing is applied at a length scale that is ten times smaller than the computational domain, so that large-scale dynamo action

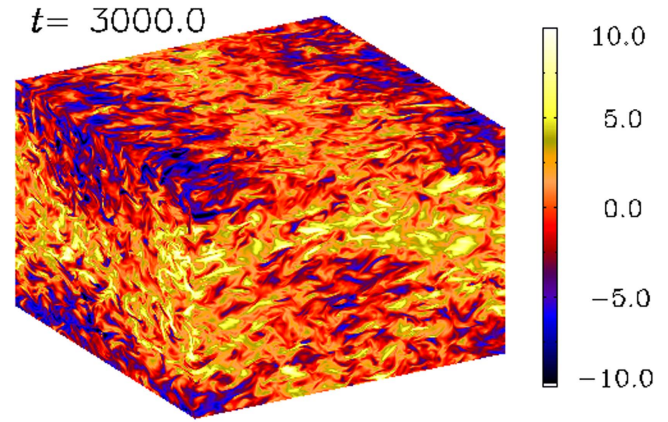


Figure 3. Visualization of B_x on the periphery of the domain. The z direction points upward, and the equatorial plane is in the middle of the domain. Note the occurrence of a large-scale magnetic field patches together with a small-scale field on the scale of the forcing.

on the scale of the domain is possible. The helicity of the forcing function is proportional to $\sin K_0 z$, where $K_0 = 2\pi/L$ is the smallest wavenumber in our domain of size L^3 . To illustrate the appearance of such a field, we show in Figure 3 the component B_x on the periphery of the domain for a simulation with 576^3 meshpoints at a magnetic Reynolds number, $R_m = u_{\text{rms}}/\eta k_f \approx 100$, where u_{rms} is the rms velocity of the turbulence, η is the magnetic diffusivity, and k_f is the forcing wavenumber with $k_f \approx 10 K_0$. The magnetic Prandtl number is $\text{Pr}_M = \nu/\eta = 1$, where ν is the kinetic viscosity. The setup of these simulations is similar to that of Mitra et al. (2010), who found that such Cartesian dynamos with an equator produce helical magnetic fields with equatorward migration, if the magnetic boundaries in the z direction are perfect conductors. In the present case, on the other hand, a periodic boundary condition is used. The present simulation has been performed with the Pencil Code.⁶

In Figure 4 we show xz slices and averages of both kinetic and current helicities (i.e., $\boldsymbol{\omega} \cdot \mathbf{u}$ with $\boldsymbol{\omega} = \nabla \times \mathbf{u}$ being the vorticity, and $\mathbf{J} \cdot \mathbf{B}$, respectively). The averages are taken along the direction normal to the plane. The four panels show that both kinetic and current helicities are negative above the midplane ($0 < z < \pi$) and positive below ($-\pi < z < 0$). However, the individual slices show considerable fluctuations and violations of the hemispheric sign rule, even though this simulation has maximally helical forcing at $\sin K_0 z = 1$ or -1 . The averages over the normal direction are much less noisy, although fluctuations on the forcing scale can still be discerned. In Figure 5 we show $\langle \boldsymbol{\omega} \cdot \mathbf{u} \rangle_{xy}(z)$ and $\langle \mathbf{J} \cdot \mathbf{B} \rangle_{xy}(z)$ (i.e., where we have also averaged over the x direction). We clearly see the sinusoidal variation of the two mean helicity densities, just like in panel (b) of Figures 1 and 2. The inset of Figure 5 shows that $\langle \mathbf{A} \cdot \mathbf{B} \rangle_{xy}(z)$, which is dominated by the large-scale field (Brandenburg 2001), has (as expected) the opposite sign.

To verify that the bihelical signature of dynamo-generated magnetic fields can clearly be extracted from single slices of the entire volume from simulated magnetic field data, we plot in Figure 6 magnetic energy and helicity spectra. In panel (a) we plot the usual ($K = 0$) magnetic energy spectrum, $2\tilde{E}_M(0, k)$, which shows the energy injection scale at $k/K_0 = 10$, as well as magnetic energy on the scale of the

⁶ <https://github.com/pencil-code>

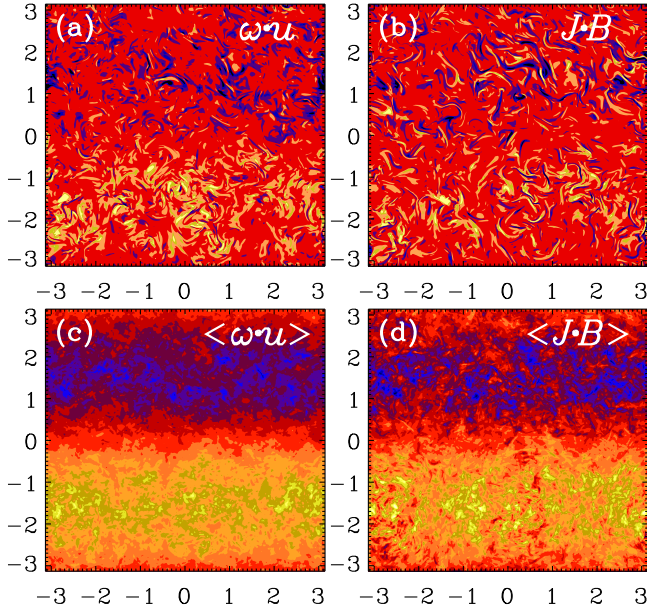


Figure 4. Slices (upper row) and averages (lower row) of $\omega \cdot u$ (left) and $J \cdot B$ (right). As in Figure 3, blue (yellow) denotes negative (positive) values.

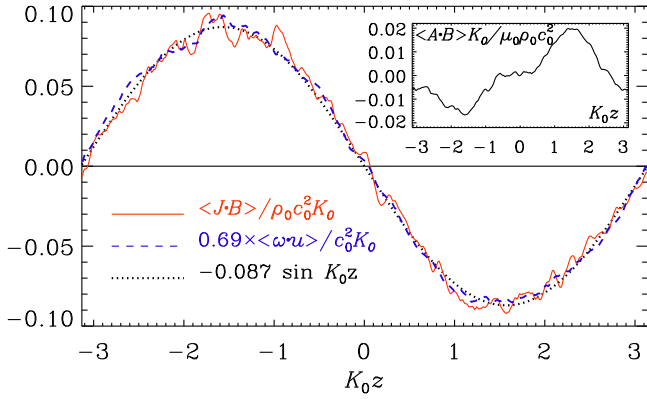


Figure 5. Dependence of $\langle J \cdot B \rangle$ and $\langle \omega \cdot u \rangle$ on z . The inset shows $\langle A \cdot B \rangle$.

domain at $k/K_0 = 1$ and 2. The scaled magnetic helicity spectrum $-\text{Im}k\tilde{H}_M(K, k)$ for $K = K_0$ can be positive and negative, so we plot $|\text{Im}k\tilde{H}_M(K_0, k)|$, but indicate the two signs using different plot symbols.

At wavenumbers above the injection wavenumber, the magnetic energy spectrum shows an approximate $k^{-5/3}$ subrange. Furthermore, $|\text{Im}k\tilde{H}_M|$ shows a $k^{-8/3}$ subrange, which corresponds to a $k^{-5/3}$ spectrum for the current helicity, as has been found previously using the usual helicity spectra in fully homogeneous turbulence (Brandenburg & Subramanian 2005; Brandenburg 2009). This variation should therefore be well suited for analysis with the two-scale approach. Note also that $|\text{Im}k\tilde{H}_M|$ reaches peak values at around 0.003, which is somewhat below the typical value of $|\langle A \cdot B \rangle_{xy}(z)|$; see the inset of Figure 5.

In Figure 6(b) we compare current helicity spectra for $K = K_0$ and $K = 0$ (i.e., $-\text{Im}k^2\tilde{H}_M(K_0, k)$ and $\text{Re}k^2\tilde{H}_M(0, k)$, respectively), computed for six uniformly separated horizontal planes. Note that for the latter, the contributions from the planes above and below $z = 0$ tend to cancel and fluctuate around zero. The k^2 factor has been applied to show more clearly the relative strengths of the two extrema.

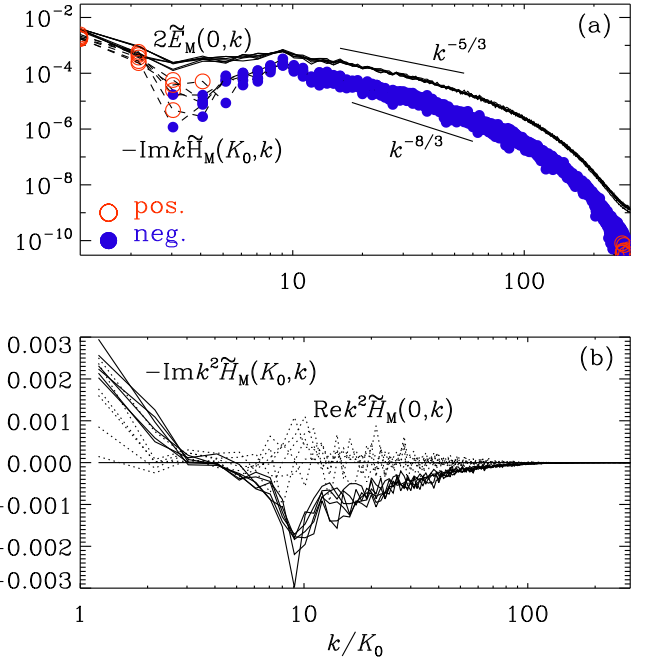


Figure 6. (a) Magnetic energy and helicity spectra from six 2D slices for 3D turbulence. (b) Comparison between $-\text{Im}k^2\tilde{H}_M(K_0, k)$ (solid lines) and $\text{Re}k^2\tilde{H}_M(0, k)$ (dotted lines).

4. Application to Solar Vector Magnetograms

We combine synoptic vector magnetogram from three successive Carrington rotations (CRs). Synoptic vector magnetograms, based on full-disk vector magnetograms from the synoptic vector magnetograms from the Synoptic Optical Long-term Investigations of the Sun (SOLIS) vector spectromagnetograph (VSM), were first presented by Gosain et al. (2013). Here we consider similar but higher-resolution ($0'.1$ at the equator) synoptic maps for CR 2161–2163, constructed using full-disk vector magnetograms obtained from *SDO/HMI*. The data were processed by Yang Liu⁷ (Stanford). It is worth noting that similar data, accompanied by uncertainty maps but processed at lower intermediate resolution (1°), are also available (Hughes et al. 2016).

The magnetic field vector is expressed in spherical coordinates, (B_r, B_θ, B_ϕ) , where (r, θ, ϕ) correspond to radius r , colatitude θ , and longitude ϕ . We map the field onto the (ϕ, μ) plane, where $\mu = \cos \theta$ increases from south to north. This allows us to adopt a Cartesian analysis by substituting

$$(\phi, \mu) \rightarrow (y, z), \quad (B_r, B_\phi, -B_\theta) \rightarrow (B_x, B_y, B_z). \quad (20)$$

This mapping preserves the right-handedness of the coordinate system. We regard this approach as a substitute to what should ultimately be done in spherical harmonics, but that would be technically rather different from the previous test cases and will therefore be avoided here. Furthermore, the use of μ instead of θ is not rigorously justified, but it seems useful because it does de-emphasize in a natural way data from high latitudes that are more uncertain.

⁷ <http://hmi.stanford.edu/hminuggets/?p=1689>

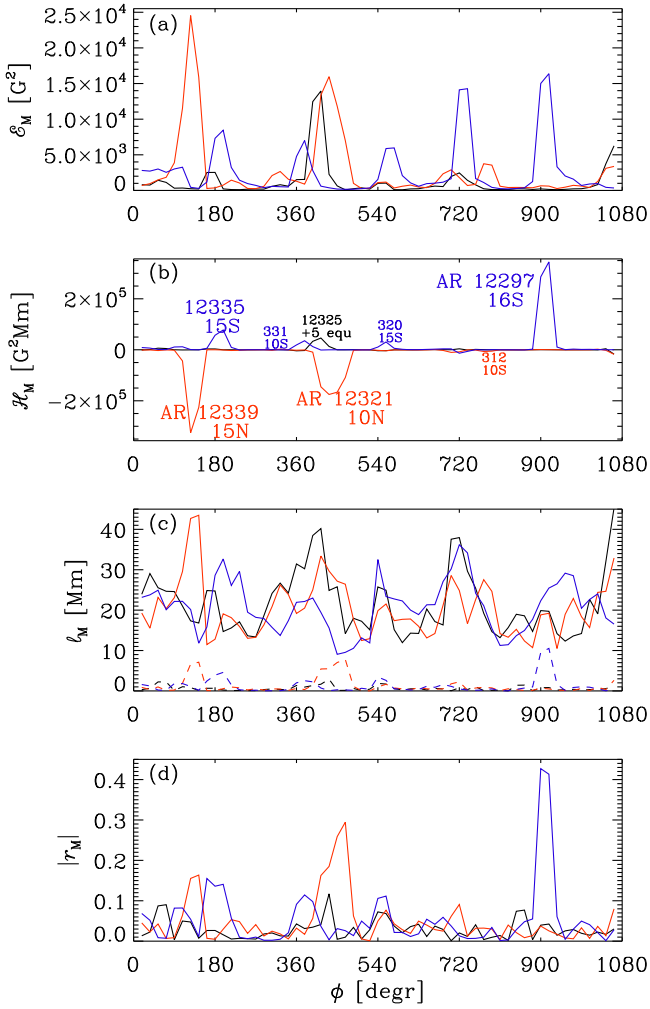


Figure 7. (a) \mathcal{E}_M , (b) \mathcal{H}_M , (c) ℓ_M (solid lines) and $|\mathcal{H}_M|/2\mathcal{E}_M$ (dashed lines), and (d) $|r_M|$ in three strips between 5° and 35° northern latitude (N, red lines), between 5° and 35° southern latitude (S, blue lines), and at the equator between $\pm 7^\circ$ latitude (E, black lines) for CR 2161–2163 covering the period from 2015 February 28 (right) to 2015 May 20 (left).

4.1. Local Analysis

Before applying the global two-scale analysis, we present in Figure 7 the time evolution of \mathcal{E}_M and \mathcal{H}_M , defined after Equation (5), by computing the usual magnetic helicity spectra for a sequence of 60 overlapping patches with a width of 36° in longitude along three strips between 5° and 35° north (N), 5° and 35° south (S), and an equatorial strip between $\pm 7^\circ$ latitude. Here $0^\circ \leq \phi \leq 360^\circ$ refers to CR 2163, $360^\circ \leq \phi \leq 720^\circ$ to CR 2162, and $720^\circ \leq \phi \leq 1080^\circ$ to CR 2161.

In Figure 7(c) we also plot the evolution of the so-called integral scale of the turbulence,

$$\ell_M = \int_0^\infty k^{-1} \tilde{E}_M(0, k) dk / \int_0^\infty \tilde{E}_M(0, k) dk, \quad (21)$$

and compare with $|\mathcal{H}_M|/2\mathcal{E}_M \leq \ell_M$, which is known as the realizability condition (Kahnashvili et al. 2013). The modulus of the ratio $r_M = \mathcal{H}_M/2\ell_M\mathcal{E}_M$ can reach values of the order of 0.15–0.4 (see Figure 7(d)).

It turns out that in most of the patches, the mean magnetic helicity is very small, and large values are confined to just a few isolated patches with strong ARs, where the magnetic helicity is large; see Figure 7(b). There are two strong ARs in

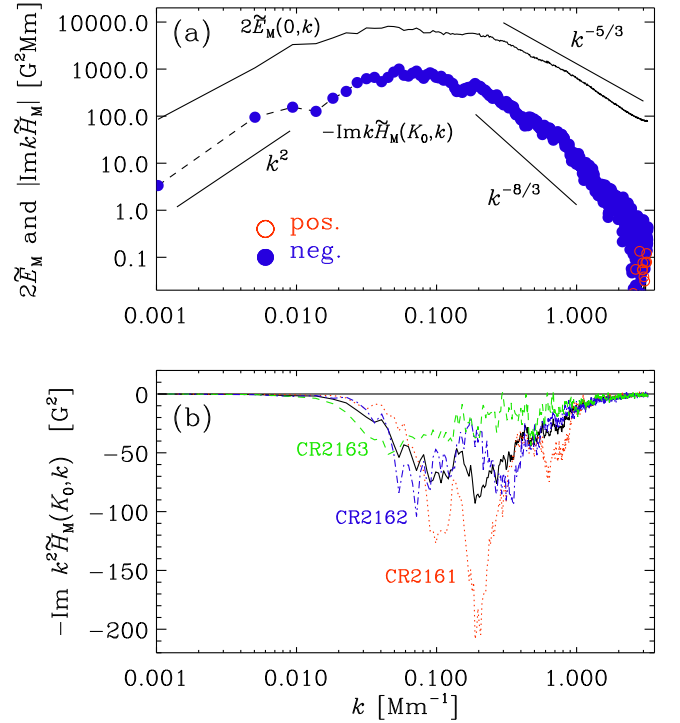


Figure 8. (a) Magnetic energy and helicity spectra for the 2D solar surface for the interval spanning CR 2161–2163. (b) Current helicity spectrum, $-\text{Im} k^2 \tilde{H}_M(K_0, k)$, for the interval spanning CR 2161–2163 (solid black) together with the results for CR 2161 (dotted red), 2162 (dashed-dotted blue), and 2163 (dashed green).

the northern hemisphere (AR 12321 and AR 12339) and one strong one in the southern hemisphere during CR 2161—namely, AR 12297. The magnetic helicity of all the other ARs is fairly weak, although there are many occasions where there are prominent ARs.

4.2. Global Analysis

Next, we consider magnetic helicity spectra obtained in the two-scale approach. In the Cartesian approach described previously, the calculation of $kH_M(\mathbf{K}, k)$ is straightforward. We consider $kH_M(\mathbf{K}, k)$ versus k for a fixed vector $\mathbf{K} = (0, K_0)$, that is, we assume that there is no systematic modulation in longitude and that $K_0 = 2\pi/2R_\odot = \pi/R_\odot$ is the projected range for $-1 \leq \mu \leq 1$, where R_\odot is the solar radius. In the following, we therefore write for simplicity $H_M(K, k)$, that is, with a scalar K . For the energy spectrum, we consider, as before, no modulation and thus just $2E(0, k)$ versus k . The highest wavenumber corresponding to the resolution of 0.1° (or 1.2 Mm) is $k_{\text{max}} = 1800/R_\odot \approx 2.6 \text{ Mm}^{-1}$.

As explained in Section 3.1, with the equator being at $\mu = 0$, the relevant quantity in this case is $-\text{Im} k \tilde{H}_M(K_0, k)$. It turns out that it is negative for almost all values of k (see Figure 8(a)). This is surprising and quite different from the corresponding result for a helically driven large-scale dynamo. Nevertheless, there are considerable variations in the value of the spectrum if one compares with data from only one of any of the three CRs. Those results are also shown in Figure 8(b). The range of variation can be regarded as an estimate of the error “bar” of $-\text{Im} k \tilde{H}_M(K_0, k)$. However, even though this quantity can change by a factor of 2, the sign still does not change.

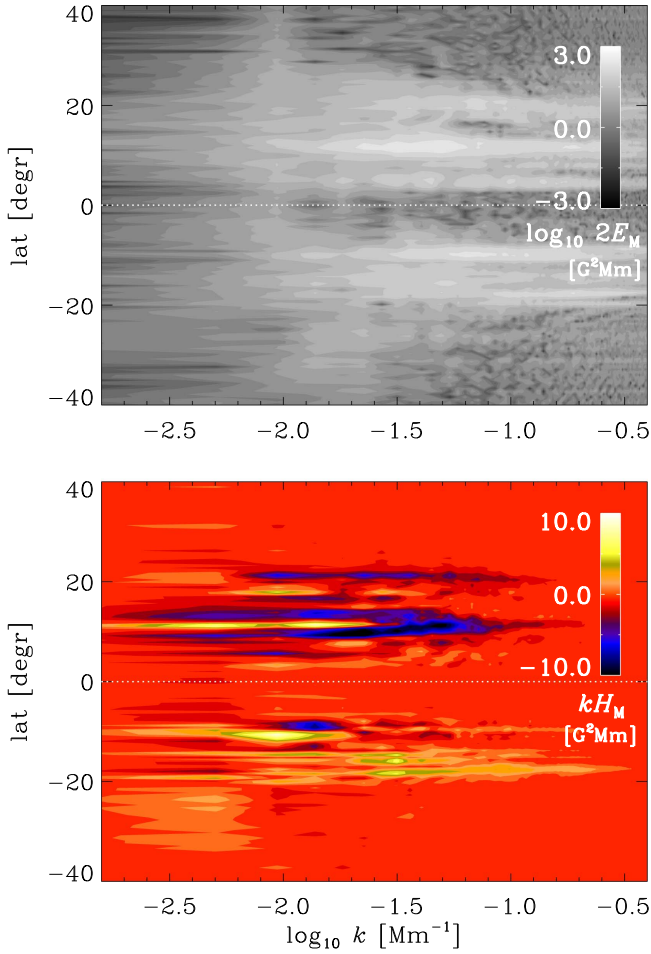


Figure 9. Magnetic energy and helicity spectra for 2D solar surface data for CR 2161–2163 as a function of k and latitude, $\arcsin Z$.

If $K_0 = 0$, we can apply the realizability condition, $|k\tilde{H}_M(0, k)| \leq 2\tilde{E}_M(0, k)$. By contrast, for $K_0 \neq 0$, this no longer holds, so the separation between the graphs of $|\text{Im}k\tilde{H}_M(K_0, k)|$ and $2\tilde{E}_M(0, k)$ can no longer be used as a quantitative measure of the fractional magnetic helicity and how close it is to the maximum possible value.

4.3. Latitudinal Dependence

Finally, let us consider the latitudinal dependence, $\mathbf{X} = (0, Z)$, at the solar surface. To do this, we have to transform back from K -space to Z -space and then plot the spectra as a function of Z (or z , or even μ , which are all equivalent). The result is shown in Figure 9, where we have computed the return transformation as

$$H_M(Z, k) = \int e^{ik_z Z} \tilde{H}_M(K_Z, k) dK_Z. \quad (22)$$

We have computed the return transformation for $E_M(Z, k)$ analogously. Here the Fourier integral has been evaluated as a Fast Fourier Transform with $-128 \leq K/K_0 \leq 127$, resulting in 256 points in $-1 < \mu < 1$. It turns out that both $kH_M(Z, k)$ and $2E_M(Z, k)$ are strongly concentrated along narrow latitudinal strips at $\pm 15^\circ$ latitude. Again, the spectra are concentrated within the range $0.01 \text{ Mm}^{-1} \leq k \leq 0.1 \text{ Mm}^{-1}$. As expected, the magnetic helicity is negative in the north, which is consistent with the two-scale analysis, where a

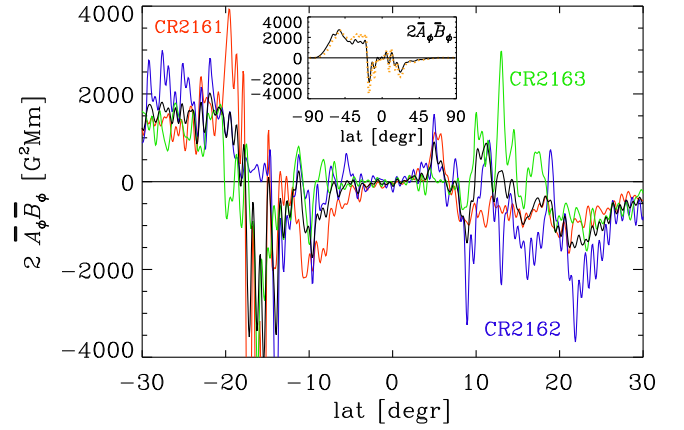


Figure 10. Latitudinal dependence of $2\bar{A}_\phi\bar{B}_\phi$ for CR 2161–2163 (black), together with the results for the three CRs separately. The inset shows the full range from pole to pole (black) and a comparison with the result from the Cartesian analysis (orange dashed).

negative value of $\text{Im}\tilde{H}(K_0, k)$ corresponds to negative magnetic helicity in the north and positive in the south.

Let us emphasize at this point that by going into Fourier space, we have automatically eliminated the gauge dependence of magnetic helicity. This, in turn, is a consequence of the implicit assumption that the input to the Fourier transform is periodic. This assumption might reasonably well be justified if the domain extends between both poles, where the field is weak anyway, and in longitude, if sufficiently many synoptic maps are “stitched” together. Ultimately, of course, the Fourier formalism should be replaced by one involving spherical harmonics, similar to what has been done previously for the mean magnetic field (Brandenburg et al. 2003; Pipin & Pevtsov 2014). However, this has not yet been developed in the context of the two-scale formalism.

4.4. Comparison with the Azimuthally Averaged Mean Field

Let us now compare with the magnetic helicity density from the azimuthally averaged mean magnetic field, $\bar{\mathbf{B}} = \int_0^{2\pi} \mathbf{B} d\phi / 2\pi$, for which the gauge-invariant relative magnetic helicity is given by $2 \int \bar{A}_\phi \bar{B}_\phi d^Dx$ (Brandenburg et al. 2002), where \bar{A}_ϕ and \bar{B}_ϕ are the toroidal components of $\bar{\mathbf{A}}$ and $\bar{\mathbf{B}} = \nabla \times \bar{\mathbf{A}}$, respectively, and $\bar{A}_\phi = \bar{B}_\phi = 0$ on the axis. We now compute the magnetic helicity density, $2\bar{A}_\phi\bar{B}_\phi$, where \bar{A}_ϕ is related to $\bar{B}_r = -\partial(\sin\theta\bar{A}_\phi)/\partial\mu$. Analogously, in our Cartesian mapping, we have $\bar{B}_x = -\partial\bar{A}_y/\partial z$.

To compute \bar{A}_y , it is convenient to employ spectral space (i.e., $\hat{A}_y = -\hat{B}_x/ik_z$ in our mapping). Alternatively, in spherical coordinates, owing to axisymmetry, we have (Brandenburg et al. 2003; Pipin & Pevtsov 2014)

$$\bar{A}_\phi(\mu) = -R \sum_{\ell=1}^{N_\ell} \frac{\ell + 1/2}{\ell(\ell + 1)} \hat{B}_\ell P_\ell^1(\mu), \quad (23)$$

where $P_\ell^1(\mu)$ are the associated Legendre polynomials of degree ℓ and order one, $\hat{B}_\ell = \int_{-1}^1 \bar{B}_r(\mu) P_\ell(\mu) d\mu$ are the coefficients in a series in terms of the Legendre polynomials $P_\ell(\mu)$, and N_ℓ is the truncation (see Rädler (1973) or Krause & Rädler (1980) for details). Using $N_\ell = 500$, the result for $2\bar{A}_\phi\bar{B}_\phi$ is given in Figure 10, where we show its latitudinal dependence either for the combined data set of CR 2161–2163 or for each of the three

CRs separately. Here, \hat{B}_ϕ has been truncated to the same level using an equation analogous to Equation (10), but with expansion coefficients computed with $P_\ell^1(\mu)$ instead of $P_\ell(\mu)$.

It turns out that at -15° latitude the magnetic helicity density is mostly negative, but at $+15^\circ$ latitude it is more noisy and with positive values only for CR2163 and mostly negative values for CR2162. The inset shows the full latitudinal extent and a comparison with the corresponding Cartesian result. Here we have applied a low-pass filter with $|k_z| \leq 0.1 \text{ Mm}^{-1}$, corresponding to $N_\ell = 70$. The Cartesian result agrees with the spherical harmonics reconstruction. Both show large positive contributions throughout the southern hemisphere. Those are caused by the systematic presence of radial fields ($\bar{B}_r \approx -5 \text{ G}$) at 50° – 80° southern latitudes.

The values of $2|\bar{A}_\phi \bar{B}_\phi|$ are of the order of $1000 \text{ G}^2 \text{ Mm}$, which is comparable to the values of $|kH_M(k)|$ near the maximum at $k = 0.1 \text{ Mm}^{-1}$; see Figure 8. This suggests that the contributions from the azimuthally averaged mean field are captured correctly by our two-scale analysis. On the other hand, there is an obvious difference between these two approaches, in that in our two-scale approach the gauge analogous to $A_\phi(\mu = \pm 1) = 0$ is not adopted, but instead the integral over $A_\phi(\mu)$ is implicitly assumed to vanish. This can cause a difference in the $k \rightarrow 0$ limit.

5. Comparison with Earlier Work

Although the use of a two-scale analysis is completely new in solar physics, some meaningful comparison with earlier work can be made. First, the fact that the magnetic helicity is negative in the north and positive in the south has been known for some time (Seehafer 1990; Pevtsov et al. 1995; Bao et al. 1999), but the global analysis is now able to show that, averaged over one or several CRs, there are hardly any sign changes in one hemisphere (i.e., the hemispheric sign rule of magnetic helicity is well obeyed). The average spectral current helicity at $k = 0.1 \text{ Mm}^{-1}$ (a scale of approximately 60 Mm) is about -100 G^2 in the northern hemisphere (see Figure 8(b)). Such a statement has not been possible with conventional methods, which were restricted to just the area of one AR. For example, the approach of Zhang et al. (2016) yielded values of about 10^3 G^2 for AR 11158 and 10^4 G^2 for AR 11515, both in the southern hemisphere and at $k = 0.1 \text{ Mm}^{-1}$. These values are between 10 times (for AR 11158) and 100 times (for AR 11515, which had exceptionally large helicity) larger than the averaged spectral current helicity found here for the entire Sun.

Most of the earlier work on magnetic helicity measurements was restricted to the total magnetic helicity over all wavenumbers and for a finite volume around a given AR. Such an approach involves either time integration of photospheric magnetic helicity injection or force-free field extrapolation, both of which are time consuming; see Valori et al. (2016) for a review. Nevertheless, as already demonstrated by Zhang et al. (2014), such values of total magnetic helicity are similar to the magnetic helicity density around a given patch, for example, if one assumes a volume of $3 \times 10^6 \text{ Mm}^3$ given by the area of the patch of $(186 \text{ Mm})^2$ and a height of 100 Mm. For the spectrum of AR 11158, the spectral current helicity density of 10^3 G^2 corresponds to a mean magnetic helicity of about $3 \times 10^4 \text{ G}^2 \text{ Mm}$; see also Figure 3 of Zhang et al. (2016). Thus the total magnetic helicity is $10^{11} \text{ G}^2 \text{ Mm}^4$. Since $1 \text{ G}^2 \text{ Mm}^4 = 10^{32} \text{ Mx}^2$, it corresponds to 10^{43} Mx^2 ; this agrees

with earlier estimates of the gauge-invariant magnetic helicity for this AR, using time integration of photospheric magnetic helicity injection (Liu & Schuck 2012; Vemareddy et al. 2012) and nonlinear force-free coronal field extrapolation (Jing et al. 2012; Tziotziou et al. 2013).

The main advantage of our approach is that it can readily be applied to global measurements covering all longitudes and latitudes over both hemispheres at the same time. In that way, one can efficiently average over fluctuations, especially in cases when there is significant cancellation. An example of this type is AR 11515, which was an extremely complex AR with a significant amount of magnetic helicity cancellation (Wang et al. 2014; Lim et al. 2016). Moreover, even though it occurred in the southern hemisphere, the net magnetic helicity was negative (Lim et al. 2016), which was explained by a significant amount of oppositely signed magnetic helicity at large length scales (Zhang et al. 2016). Curiously, however, the presence of an oppositely signed magnetic helicity at large length scales in AR 11515 of 2012 July 6 is not borne out by the present work. This highlights the importance of applying our new approach to longer time series covering also a range of different phases of the solar cycle.

6. Conclusions

The present work has shown that it is possible to generalize the notion of a helicity spectrum to the case where the helicity is locally modulated in a large-scale fashion, which may even include a sign change. This approach is particularly useful for characterizing the spectrum of solar magnetic helicity, with the aim of being able to find out whether there is evidence for a bihelical spectrum. Bihelical spectra have been seen in turbulent dynamo simulations where turbulence is driven by a helical forcing function. Surprisingly, our present results suggest that, for the Sun, the helicity spectrum is not bihelical—at least not at the surface. The reason for this is not understood at present. As we have shown in Figure 10, the contribution from the azimuthally averaged mean field is of comparable magnitude to that from our two-scale analysis, but it is very noisy and has only in the southern hemisphere at -15° significant negative contributions, which would be in agreement with Pipin and Pevtsov (2014) and perhaps suggestive of a bihelical field. However, this contribution is overwhelmed by much stronger contributions of the opposite sign at latitudes south of -40° . It might well be that our time frame was unfortunate and that the net magnetic helicity of the large-scale field was close to zero. Another possibility is that the weak contribution of large-scale fields with opposite sign is just a surface effect. Observations of the magnetic field in the solar wind have indicated the presence of a bihelical spectrum (Brandenburg et al. 2011) and that the signs of the two contributions at large and small scales are the other way around than what is expected inside the Sun. One is therefore led to consider the possibility of the spectrum having changed along the way since it left the Sun, which is indeed what turbulence simulations (Warnecke et al. 2011) and mean-field models (Bonanno 2016). The role of the surface has yet to be studied in that respect, but there is clearly now a need to consider theoretical models of global convection-driven dynamos and to apply the two-scale approach to different layers: the surface, the interior of the convection zone, and an outer coronal layer.

We thank the referee for useful suggestions and Yang Liu (Stanford University) for providing us with the synoptic vector magnetograms used in the present paper. This work utilizes *SOLIS* data obtained by the NSO Integrated Synoptic Program (NISP), managed by the National Solar Observatory, which is operated by the Association of Universities for Research in Astronomy (AURA), Inc., under a cooperative agreement with the National Science Foundation. *SDO* is a mission for NASA's Living with a Star program. This work has been supported in part by the Swedish Research Council grant No. 621-2011-5076 and the Research Council of Norway under the FRINATEK grant No. 231444.

Appendix Derivation of Equations (17) and (18)

The purpose of this appendix is to present the derivation of Equations (18) and (19). The Fourier transform of \mathbf{B} yields

$$\hat{\mathbf{B}}(k) = \frac{1}{2}(\delta_k k_1^- + \delta_{-k} k_1^-, \delta_k k_1^+ + \delta_{-k} k_1^+, 0). \quad (24)$$

We recall that in 1D, the integrals in Equations (14) and (15) still extend over positive and negative values of k . Thus the surface integral reduces to a sum of two contributions, one with positive k and one with negative k . For $K = 0$, Equation (14) yields

$$\begin{aligned} 2\tilde{E}_M(0, k) &= \frac{1}{4}(\delta_{k'} k_1^+ + \delta_{-k'} k_1^+) \Big|_{k'=-k} \\ &\quad + \frac{1}{4}(\delta_{k'} k_1^- + \delta_{-k'} k_1^-) \Big|_{k'=k} \\ &= \frac{1}{2}(\delta_k k_1^+ + \delta_k k_1^-), \end{aligned} \quad (25)$$

which is in agreement with Equation (18) and Figure 1. Here, the $1/4$ factor is the energy of each Fourier peak, but there are two of them at $k = \pm k_1^-$ and at $k = \pm k_1^+$, which explains the $1/2$ amplitudes of each of the peaks in energy.

Next, we calculate $k\tilde{H}_M(K_0, k)$. Since $\hat{\mathbf{k}}$ has only a z component, Equation (15) yields

$$\begin{aligned} k\tilde{H}_M(K_0, k) &= i\hat{k}'[\tilde{M}_{xy}(K_0, k') - \tilde{M}_{yx}(K_0, k')] \Big|_{k'=-k} \\ &\quad + i\hat{k}'[\tilde{M}_{xy}(K_0, k') - \tilde{M}_{yx}(K_0, k')] \Big|_{k'=k}. \end{aligned} \quad (26)$$

To compute $\tilde{M}_{xy}(K_0, k)$ and $\tilde{M}_{yx}(K_0, k)$, we need the Fourier transforms shifted by $\pm K_0/2$. Those are given by

$$\hat{\mathbf{B}}\left(k + \frac{1}{2}K_0\right) = \frac{1}{2} \begin{pmatrix} \delta_k k_1 - K_0 + \delta_{-k} k_1 \\ \delta_k k_1 + \delta_{-k} k_1 + K_0 \\ 0 \end{pmatrix}, \quad (27)$$

$$\hat{\mathbf{B}}\left(k - \frac{1}{2}K_0\right) = \frac{1}{2} \begin{pmatrix} \delta_k k_1 + \delta_{-k} k_1 - K_0 \\ \delta_k k_1 + K_0 + \delta_{-k} k_1 \\ 0 \end{pmatrix}. \quad (28)$$

Thus $\tilde{M}_{xy}(K_0, k) = \frac{1}{4}\delta_{-k} k_1$ and $\tilde{M}_{yx}(K_0, k) = \frac{1}{4}\delta_k k_1$. Therefore, Equation (26) yields

$$\begin{aligned} k\tilde{H}_M(K_0, k) &= \frac{1}{4}i\hat{k}'\delta_{-k'} k_1 \Big|_{k'=-k} - \frac{1}{4}i\hat{k}'\delta_{k'} k_1 \Big|_{k'=k} \\ &= -\frac{1}{2}i \operatorname{sgn}(k_1)\delta_k k_1. \end{aligned} \quad (29)$$

This is in agreement with Equation (19).

References

- Abramenko, V. I. 2005, *ApJ*, 629, 1141
 Amari, T., Canou, A., & Aly, J.-J. 2014, *Natur*, 514, 465
 Bao, S. D., Zhang, H. Q., Ai, G. X., & Zhang, M. 1999, *A&A*, 139, 311
 Blackman, E. G., & Brandenburg, A. 2003, *ApJL*, 584, L99
 Bonanno, Y. 2016, *ApJL*, 833, L22
 Brandenburg, A. 2001, *ApJ*, 550, 824
 Brandenburg, A. 2009, *ApJ*, 697, 1206
 Brandenburg, A., Blackman, E. G., & Sarson, G. R. 2003, *AdSpR*, 32, 1835
 Brandenburg, A., Dobler, W., & Subramanian, K. 2002, *AN*, 323, 99
 Brandenburg, A., & Subramanian, K. 2005, *A&A*, 439, 835
 Brandenburg, A., Subramanian, K., Balogh, A., & Goldstein, M. L. 2011, *ApJ*, 734, 9
 Field, G. B., & Blackman, E. G. 2002, *ApJ*, 572, 685
 Gosain, S., Pevtsov, A. A., Rudenko, G. V., & Anfinogentov, S. A. 2013, *ApJ*, 772, 52
 Gruzinov, A. V., & Diamond, P. H. 1996, *PhPl*, 3, 1853
 Hughes, A. L. H., Bertello, L., Marble, A. R., et al. 2016, arXiv:1605.03500
 Ji, H. 1999, *PhRvL*, 83, 3198
 Jing, J., Park, S.-H., Liu, C., et al. 2012, *ApJL*, 752, L9
 Kahniashvili, T., Tevzadze, A. G., Brandenburg, A., & Neronov, A. 2013, *PhRvD*, 87, 083007
 Kleorin, N. I., & Ruzmaikin, A. A. 1982, *MHD*, 18, 116
 Krause, F., & Rädler, K.-H. 1980, *Mean-field Magnetohydrodynamics and Dynamo Theory* (Oxford: Pergamon)
 Lim, E.-K., Yurchyshyn, V., Park, S.-H., et al. 2016, *ApJ*, 817, 39
 Liu, Y., & Schuck, P. W. 2012, *ApJ*, 761, 105
 Low, B. C. 1994, *PhFl*, 1, 1684
 Matthaeus, W. H., Goldstein, M. L., & Smith, C. 1982, *PhRvL*, 48, 1256
 Mitra, D., Tavakol, R., Käpylä, P. J., & Brandenburg, A. 2010, *ApJL*, 719, L1
 Nakagawa, Y., & Priest, E. R. 1973, *ApJ*, 179, 949
 Nindos, A., Zhang, J., & Zhang, H. 2003, *ApJ*, 594, 1033
 Pariat, E., Valori, G., Démoulin, P., & Dalmasse, K. 2015, *A&A*, 580, A128
 Pevtsov, A. A., Berger, M. A., Nindos, A., Norton, A. A., & van Driel-Gesztelyi, L. 2014, *SSRv*, 186, 285
 Pevtsov, A. A., Canfield, R. C., & Metcalf, T. R. 1995, *ApJL*, 440, L109
 Pevtsov, A. A., Canfield, R. C., Sakurai, T., & Hagino, M. 2008, *ApJ*, 677, 719
 Pipin, V. V., & Pevtsov, A. A. 2014, *ApJ*, 789, 21
 Rädler, K.-H. 1973, *AN*, 294, 213
 Roberts, P. H., & Soward, A. M. 1975, *AN*, 296, 49
 Seehafer, N. 1990, *SoPh*, 125, 219
 Seehafer, N. 1996, *PhRvE*, 53, 1283
 Stenflo, J. O. 2012, *A&A*, 541, A17
 Tziotziou, K., Georgoulis, M. K., & Liu, Y. 2013, *ApJ*, 772, 115
 Valori, G., Pariat, E., Anfinogentov, S., et al. 2016, *SSRv*, 201, 147
 Vemareddy, P., Ambastha, A., Maurya, R. A., & Chae, J. 2012, *ApJ*, 761, 86
 Wang, H., Liu, C., Deng, N., et al. 2014, *ApJL*, 781, L23
 Warnecke, J., Brandenburg, A., & Mitra, D. 2011, *A&A*, 534, A11
 Yousef, T. A., & Brandenburg, A. 2003, *A&A*, 407, 7
 Zhang, H., Brandenburg, A., & Sokoloff, D. D. 2014, *ApJL*, 784, L45
 Zhang, H., Brandenburg, A., & Sokoloff, D. D. 2016, *ApJ*, 819, 146
 Zhang, H., Sakurai, T., Pevtsov, A., et al. 2010, *MNRAS*, 402, L30